JOURNAL OF SOLID STATE CHEMISTRY 80, 178–188 (1989)

The Structure of $Bi_{15}Ti_9Fe_{11}O_{57}$ and Related Compounds Derived by High-Resolution Electron Microscopy

MONICA LUNDBERG

Inorganic Chemistry, Arrhenius Laboratory, University of Stockholm, S-106 91 Stockholm, Sweden

JOHN L. HUTCHISON

Department of Metallurgy and Science of Materials, University of Oxford, Parks Rd., Oxford OX1 3PH, United Kingdom

AND DAVID J. SMITH

Center for Solid State Science and Department of Physics, Arizona State University, Tempe, Arizona 85287

Received July 29, 1988; in revised form February 20, 1989

The structure of a complex two-dimensional supercell observed by high-resolution electron microscopy in a layered bismuthate has been deduced from structural chemistry principles. It is proposed that this superstructure should form the basis for a new type of homologous series of related structures. An $n = 5$ member of the series, with composition $Bi_{18}Ti_9Fe_{14}O_{66}$, has been synthesized and shown to have regions with the same two-dimensional superstructure. © 1989 Academic Press, Inc.

Introduction

Complex layered bismuthates of general formula $Bi_2A_{m-2}B_{m-1}O_{3m}$, the so-called "Aurivillius phases," can be regarded as being built up from perovskite slabs linked by bismuth oxide sheets. The structural principle of these oxides is better expressed by the term

$$(Bi_2O_2)^{2+}(A_{n-1}B_nO_{3n+1})^{2-}$$

which indicates that the perovskite slabs are n octahedra in width (the "B"-site cations such as Ti^{4+}, Nb^{5+}, etc., being six-coordinate), containing $n - 1$ rows of 12-coordinated cations such as Bi^{3+} and Ba^{2+}. These phases were first identified by Aurivillius (*1*) on the basis of X-ray measurements. Members of the series for n less than or equal to 5 have now been well-characterized by electron microscopy, for a variety of A- and B-cation compositions (*2*). Efforts to prepare an $n = 8$ compound, whose existence was claimed in earlier work (*3*), have so far been unsuccessful. In the system $Bi_2CaNa_{n-2}Nb_nO_{3n+3}$, members for $n = 5$ to 8 were not well-ordered (*4*), and in the case of "$Bi_9Ti_3Fe_5O_{27}$" (a composition intended to produce Ismailzade's original "$n = 8$" compound) our initial electron microscope studies indicated that it consisted of a mixture of $n = 4$ and $n = 5$ com-

0022-4596/89 $3.00

pounds (*2*). Subsequent high-resolution investigations of this material, using the high-voltage instrument at Cambridge, confirmed this general finding but also revealed the existence of hitherto unreported structures, based on a $3 \times d_{110}$ supercell relative to the original "Aurivillius structures" (*5*). Although the projected dimensions of the cell could be derived accurately with respect to the perovskite structure in the intervening slabs, no plausible structural model was proposed at that time.

We have now completed a more thorough analysis of the micrographs and present here a model for this new superlattice structure, supported by computer image simulations. This structure forms the basis for a new homologous series. Furthermore, we have been successful in synthesizing another member of the series, not necessarily an equilibrium phase, which shows the same two-dimensional superstructure.

Experimental

Preparation of samples. The preparation of a sample of nominal composition $Bi_9Ti_3Fe_5O_{27}$ from the constituent oxides, as part of an earlier study of several Aurivillius structures, has been described elsewhere (*2*). Samples corresponding to $n = 4$, namely $Bi_{15}Ti_9Fe_{11}O_{57}$, and $n = 5$, namely $Bi_{18}Ti_9Fe_{14}O_{66}$, of the new homologous series were prepared by annealing appropriate mixtures for 7 weeks at 1050°C.

Electron microscopy. Images of the "$n = 8$" material ($Bi_9Ti_3Fe_5O_{27}$) were taken at 575 kV using the Cambridge University high-resolution electron microscope (HREM) (*6*). The new synthetic materials ($n = 4$ and 5) were examined at 300 and 400 kV using a JEM-4000EX HREM, equipped with an ultra-high-resolution objective lens polepiece ($C_s = 1.0$ mm). By reference to selected area electron diffraction patterns (omitted here), crystals were oriented with [110] parallel to the electron beam, and micrographs were usually recorded at electron-optical magnifications of 600,000×.

Results

Experimental images. As discussed in detail elsewhere (*5*), there was considerable disorder present in many of the "$n = 8$" crystals, similar to that seen in other "$n > 5$" materials, varying from sloping or sidestepping Bi_2O_2 layers, to "wavy" layers, to poorly ordered crystals. The superlattice (SL) structures were observed as individual, well-ordered crystallites, sometimes in association with regions of wavy layers, or even interspersed with "proper" Bi_2O_2 layers. There was also considerable variation in perovskite slab width between the SL layers, ranging from $n = 4$ to 12 or more; $n = 4$ or 5 were found frequently. Figure 1a shows a region of a comparatively well-ordered crystal and Fig. 1b shows an example of the SL structure. Both were recorded at close to the optimum objective lens focus.

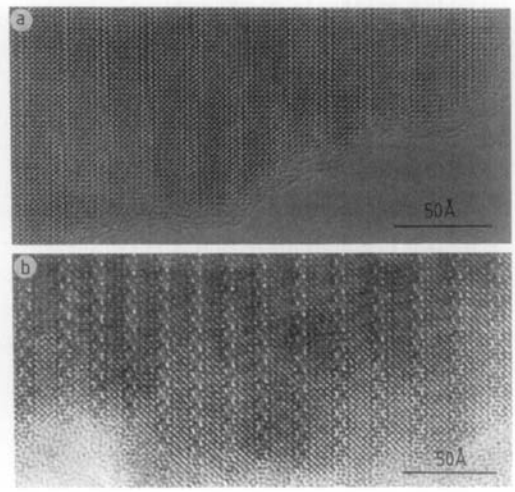

FIG. 1. (a) [110] lattice image of a typical Aurivillius phase, taken at 575 kV and optimum defocus. Dark dots correspond to projected cation positions. (b) [110] lattice image showing the "SL" structure, containing perovskite slabs four octahedra in width.

The dimensions of the SL cells could be readily determined directly from micrographs (assuming a 3.9-Å projection axis). Thus the length *a along* the SL layers corresponded to $3 \times d_{110}$ of the perovskite subcell, i.e., ~11.7 Å; *b* corresponded to the *c* parameter of the corresponding Aurivillius phase, with $c = 3.9$ Å. These dimensions were appropriate where an orthogonal cell was identified. In some instances, however, this was *not* the case, and a monoclinic cell was evident whose angle β varied with slab width. For any given slab width there would thus be more than one SL variant: an orthorhombic one with dimensions as described above and also monoclinic ones. Careful measurements of the micrographs (note that *all* projected cation sites are resolved in the micrographs) indicated that the perovskite slabs were $n - 1$ octahedra in width compared to an *n*-member Aurivillius structure. Conversely, the "Bi_2O_2" layer of nominal width 4 Å was replaced by an SL layer, 8 Å wide.

For modern HREMs, with structural information limits of better than 2 Å, it is reasonable to expect that the positions of the cation columns in oxide structures will be clearly resolved for appropriately oriented crystals. In Figs. 1a and 1b, the dark dots should thus represent projected cation columns, and this statement is supported by computer simulations (see below). Conversely, regions in these images showing white dot contrast may be correlated (in the perovskite slabs, for instance) with the anion (oxygen) sublattice (although we are not suggesting that the oxygen atomic columns are actually being resolved).

Interpretation of Image Contrast

In our approach to image interpretation, we begin with the assumption that the oxygen/Bi lattice is essentially unchanged: any arrangement of Ti and Fe cations must therefore fit into this framework with chemically reasonable coordination polyhedra. We also note that, in the imaging projection, the SL layers contain mirror planes normal to *a*, but (in projection) appear centrosymmetric. Where the SL appears orthorhombic, there is a mirror plane along the center of the perovskite slab. Any structural model for this phase must be consistent with the geometrical constraints and must, in addition, take into account crystal–chemical considerations. It must, of course, be reasonably consistent with the nominal "composition" of the starting material. (In this respect, we recognize that HREM may reveal considerable variations in local structures and compositions present in apparently homogeneous materials).

If we now consider the fine contrast details within an SL layer shown enlarged in Fig. 2, then the following features are evident:

(1) Pairs of dark dots about 2 Å apart, aligned with (the odd) rows of *B*-cation octahedra within the perovskite slabs—these are labeled "*X*." These dots form a (slightly) zigzag ladder along the SL layer.

(2) More widely spaced pairs of dots, about 3 Å apart, located between the "*X*" features. These are aligned midway between *A*-cation rows of adjacent perovskite slabs, and alternate pairs are tilted slightly

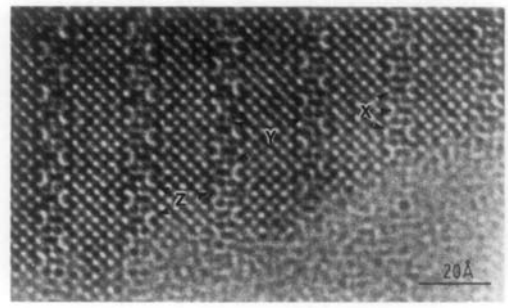

FIG. 2. Highly enlarged details of an "SL" layer. See text for interpretation of features labeled *X*, *Y*, and *Z*.

with respect to the c axis (of an orthorhombic cell). These features are labeled "*Y*."

(3) The third feature is the array of crescent-shaped light contrast areas—labeled "*Z*." At optimum defocus, these features correspond to regions of low projected potential (tunnels or oxygen sites).

Several important points emerge immediately from a consideration of the relative positions of the *X*, *Y*, and *Z* features:

(i) The $3 \times d_{110}$ repeat arises from the location of equivalent units along one side of the SL layer where it joins a perovskite slab; the repeat occurs at every *fourth* octahedron.

(ii) The arrangement of layers on either side of a slab may or may not be symmetrical, depending upon whether or not a given octahedron row terminates with (say) an *X*-unit at both ends.

(iii) The symmetry of the "repeat unit" of the SL layer becomes clear. It is obvious, for example, why there is no mirror plane *along* the layer. Pervoskite slabs on either side are displaced along the *b*-axis relative to one another (as in the Aurivillius phases).

We are now in a position to attempt to interpret these features in terms of possible structures.

(a) *X-features*. These generally appear with elongated dark contrast, often being resolved into two dark dots ~2 Å apart. As the directly interpretable image resolution of both microscopes was better than 2 Å, it is reasonable to assume at this stage that the *X*-features correspond (in projection) to a pair of edge-sharing MO_6 octahedra (an octahedron body diagonal is ~3.9 Å). Successive *X*-features are displaced on either side of the median line by about 2 Å, which is consistent with their being alternatively "attached" to perovskite slabs on one side or the other of the SL layer, as represented schematically in Fig. 3a.

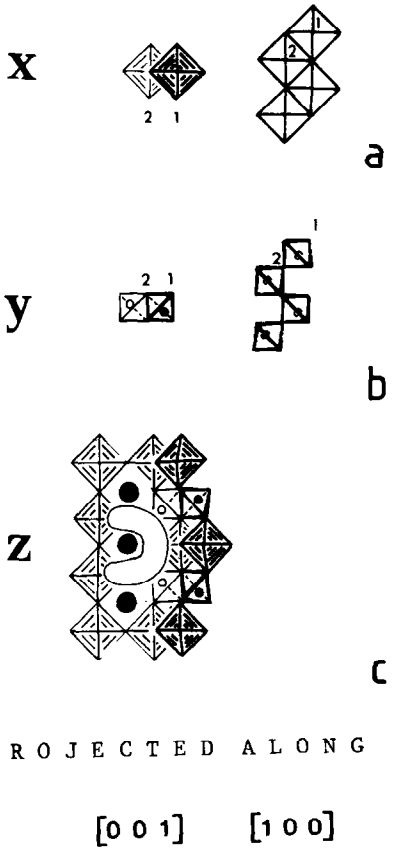

FIG. 3. Derivation of structures for different contrast features: (a) *X*, (b) *Y*, and (c) *Z*.

(b) *Y-features*. It can be seen that the assignment of pairs of edge-sharing octahedra to the *X*-features allows the anion sublattice to remain intact. If this oxygen array is now completed, as in Fig. 3b, then pairs of tetrahedral sites become evident, linking successive pairs of octahedra. If cations (Fe^{3+}) are located in these tetrahedral sites, the resultant zigzag chains of tetrahedra, seen end-on in this projection, will have columns of cations 3 Å apart. The geometrical arrangement of these exactly matches the *Y*-features in the micrographs.

(c) *Z-features*. The prominent light contrast areas labeled "*Z*" are now readily explained in terms of low projected poten-

tial—in this case, columns of oxygen ions. Figure 3c illustrates how the curiously shaped bright contrast features may be expected to arise under optimum imaging conditions.

It is now possible to propose a structure for the complete unit cell which is entirely consistent with all the observed features and which makes no unreasonable assumptions regarding bonding or coordination polyhedra. In order to obtain likely interatomic distances within the "SL" layer, the polyhedra must become slightly distorted but, for reasons of clarity, they are drawn idealized in Fig. 4 which shows the orthorhombic variant of the $n = 4$ member of a new homologous series, with composition $Bi_{15}Ti_9Fe_{11}O_{57}$, which was later synthesized.

The possibility for monoclinic structures can also be taken into account by the model, as shown in Fig. 5. From these sketches it can be seen that, for any given n-value, there are two possible monoclinic versions, depending on the locations of equivalent units on either side of a perovskite slab; the angle β is determined by the particular linkage, and also by the width of the perovskite slab (the value of "n").

In order to confirm our interpretation of the "$n = 8$" images, extensive computer simulations were carried out using the SHRLI suite of programs (*7*). These were performed for the $n = 4$ member using orthorhombic symmetry (space group *Pmm*2) and unit cell dimensions $a = 11.7$ Å, $b = 47.8$ Å, and $c = 3.93$ Å. The atomic coordinates were deduced such that all interatomic distances within the polyhedra became similar to already established transition-metal-to-oxygen and oxygen-to-oxygen distances in both octahedra and tetrahedra (see Discussion).

Simulated images of the structure model

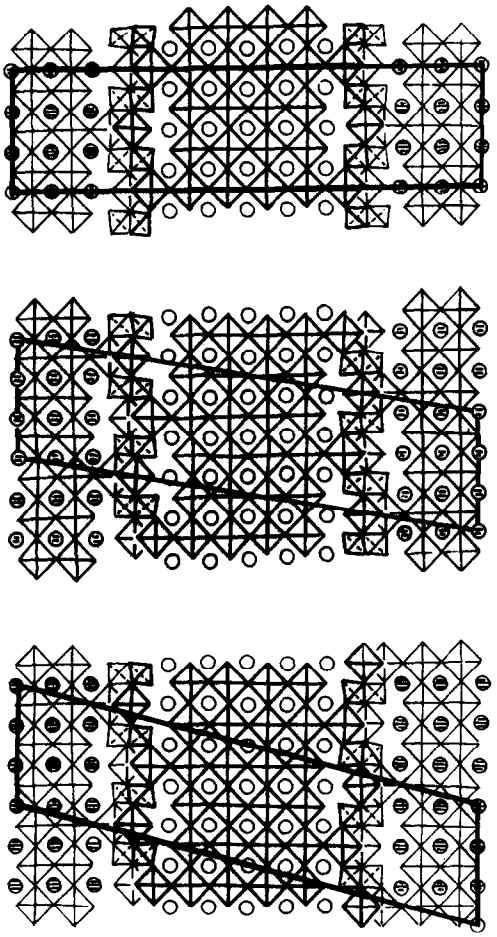

FIG. 5. Monoclinic versions of $Bi_{15}Ti_9Fe_{11}O_{57}$ drawn schematically and compared with the orthorhombic $n = 4$ variant.

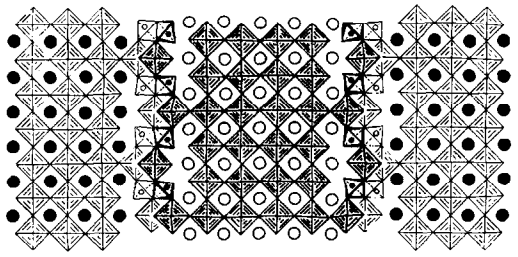

FIG. 4. Schematic showing the [110] projection of an orthorhombic version of the phase $Bi_{15}Ti_9Fe_{11}O_{57}$, the $n = 4$ member of a new homologous series. Small circles represent tetrahedrally coordinated cations.

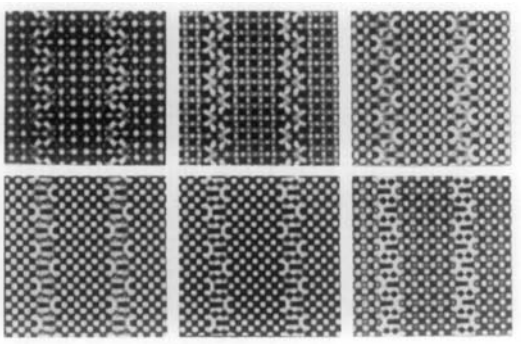

FIG. 6. Image simulations for the model structure drawn in Fig. 4, at an approximate thickness of 40 Å and defocus values (from top left to bottom right) of −100 to −600 Å. Accelerating voltage of 575 kV and spherical aberration coefficient of 2.5 mm.

drawn in Fig. 4 were calculated for crystal thicknesses of ~20 and ~40 Å at defocus values in the range of −100 to −900 Å: some examples are shown in Fig. 6. Good agreement was generally obtained between experimental micrographs and the calculated images—compare, for example, the image shown in Fig. 1b with the simulation for a thickness of 40 Å at a defocus of −500 Å (middle bottom row).

Disorder

Variations in n. In layered structures of such complexity, disorder is likely to be manifest on many different levels. In compounds belonging to homologous series, we may expect intergrowth slabs of different widths. This was indeed the case for previous investigations of the Aurivillius phases with $n > 5$ (*4*). Earlier studies of "$Bi_9Ti_3Fe_5O_{27}$," the so-called "$n = 8$" phase, also revealed this type of disorder (*5*). The new structures described in the present work display similar variations: well-ordered crystals (in terms of perovskite slab width) were frequently found but

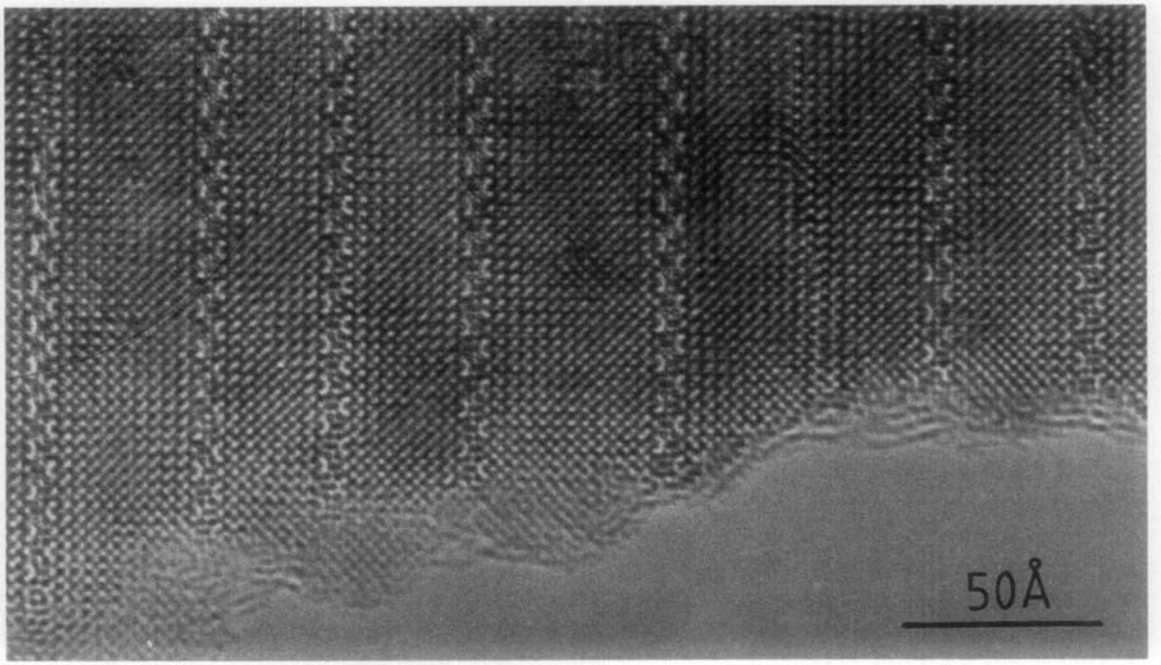

FIG. 7. High-resolution electron micrograph recorded at 575 kV showing large local variations in perovskite slab width associated with the SL phase.

examples displaying considerable variations in slab width (up to $n = 12$) were also seen, as shown in Fig. 7.

Variations in geometry. In an imperfectly ordered system, the model predicts variations in unit cell geometry with different β-angles. These are frequently found and may be regarded as simple local stacking modifications, which do not alter the local composition.

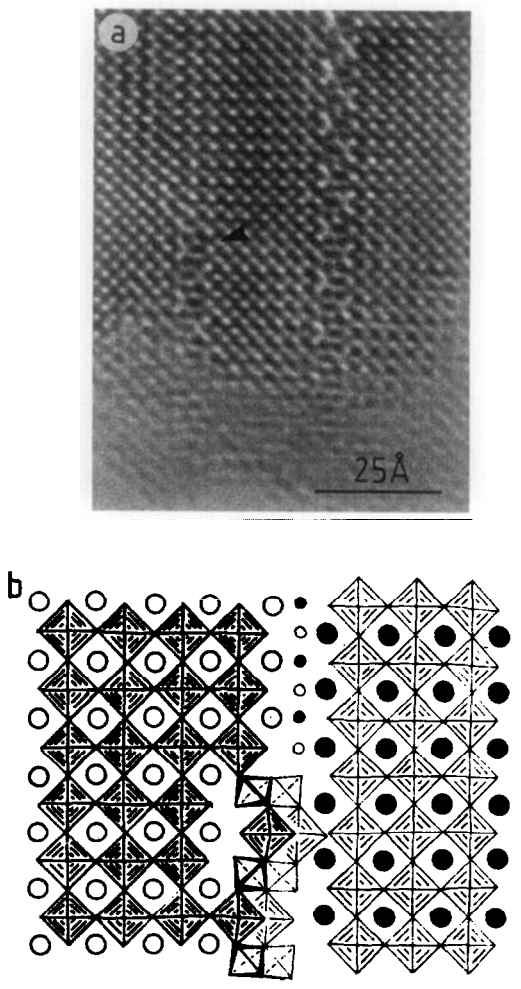

FIG. 8. (a) Structure image showing a junction between the SL layer and the bismuthate (Bi_2O_2) layer of the "normal" Aurivillius phase. (b) Proposed schematic structure of junction between a Bi_2O_2 layer and an SL layer.

Transformation faults. Evidence is occasionally found for partial transformation of the new SL structure to (or from?) an Aurivillius phase (see Fig. 4 in Ref. (*5*)). A more curious example, which confirms the idea that the SL and Aurivillius structures are closely related, is the junction arrowed in Fig. 8a. The transformation here from an "SL" layer to a Bi_2O_2 layer appears abrupt, with little detectable lattice distortion. A possible structure for this junction is drawn in Fig. 8b. It can be seen that the only alteration to the layer ordering will be a sideways displacement of about 2 Å, creating an extra row of octahedra in the left-hand perovskite slab.

"Local faults." Small defect clusters were sometimes observed, particularly along the middle of wide perovskite slabs, as shown in Fig. 9. Although these seemed, at first sight, to resemble elements of tetragonal tungsten bronze (TTB) structure, closer inspection revealed significant differences.

A satisfactory model for these clusters has been derived which retains the close packing of the oxygen/bismuth array. In thin regions of crystal, images at optimum defocus show the projected cation sites clearly. The contrast at the defects in Fig. 9 is such that the two dark features which appear displaced with respect to the perovskite structure are likely to be *A*-cations, in this case Bi^{3+}. Figure 10a shows a model for this defect which can be described as a replacement of two oxygen ions by two Bi^{3+} ions (large filled circles) located at the same height as the transition metal ions. The atomic arrangement can be considered as a twin orientation of a piece of a Bi_2O_2 layer perpendicular to the infinite Bi_2O_2 layers in the main structure.

For the purpose of verifying this model of the defect by comparison with simulated images, the defect was inserted into a perovskite matrix of 8×8 MO_6 octahedra, which resulted in the "unit cell" dimen-

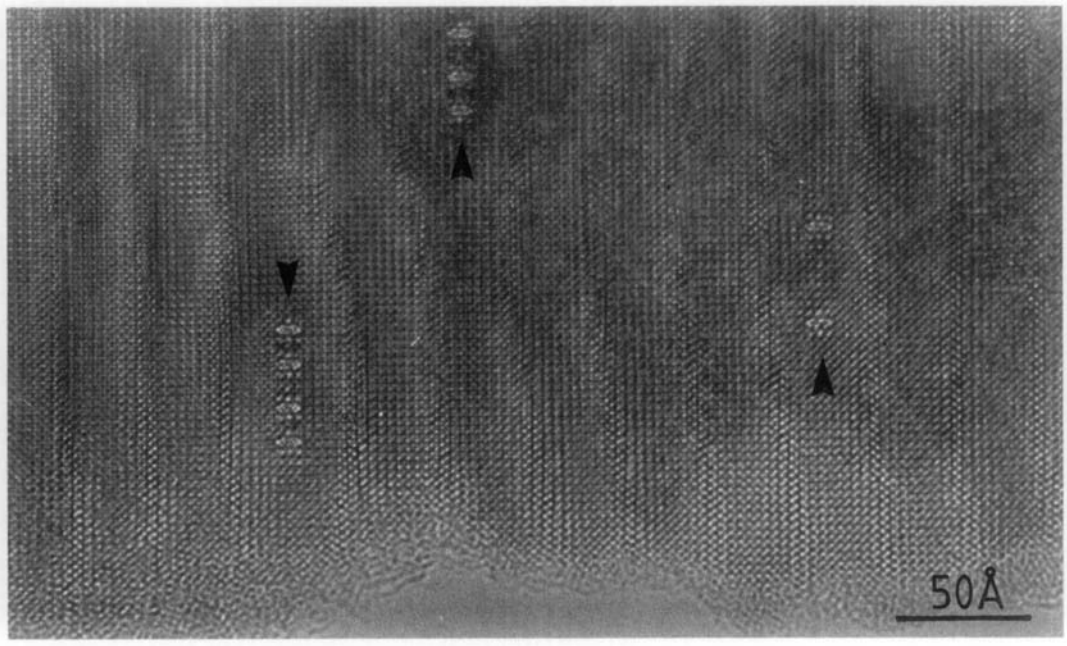

FIG. 9. Small defect clusters (arrowed) in the center of perovskite slabs in Aurivillius phase.

sions $a = b = 27.3$ Å and $c = 3.93$ Å. Orthorhombic symmetry (space group *Pmmm*) was applied to the atomic coordinates thus deduced. Image calculations were performed for crystal thicknesses of ~20, ~40, and ~60 Å and defocus values ranging from +300 to −1200 Å (see Fig. 10b). Good agreement with Fig. 9 was achieved for a 40-Å-thick crystal at a defocus of −300 Å. It is also worth mentioning that the image with reverse contrast at −1200 Å closely matched the experimental image shown in Ref. ((*5*) (at C in Fig. 7)).

Symmetry disorder. In interpreting the experimental images and deriving possible structures, the assumption was made that the perovskite slabs could be regarded as having cubic symmetry. In most perovskite compounds, however, this is not the case, and it is well known that slight distortions can lead to the formation of anti-phase and twin domains, as studied recently in $CaTiO_3$ (*8*). Although little experimental data is available for the "$Bi(Fe,Ti)O_3$" version of perovskite which comprises the slabs in the structures described in the present work, it is likely that the lone pair of electrons on Bi^{3+} will cause these species to be displaced from the central position in the *A*-sites. Combined with the octahedral distortions, the symmetry in the perovskite slabs will thus be considerably reduced.

With these considerations in mind, the curious "chevron" features which appeared in many of the slabs between the SL layers may now be tentatively interpreted. It is evident, as shown in Fig. 11a for a sample of the $n = 5$ phase, that these chevrons are aligned along rows of *A*- and *B*-cations in such a way as to form triangular domains. *Across* the domain boundaries, slight displacements in cation positions may be detected. We believe that these domains are inversion twins similar to those described elsewhere (*8*). On opposite sides of these boundaries, the Bi^{3+} cations are

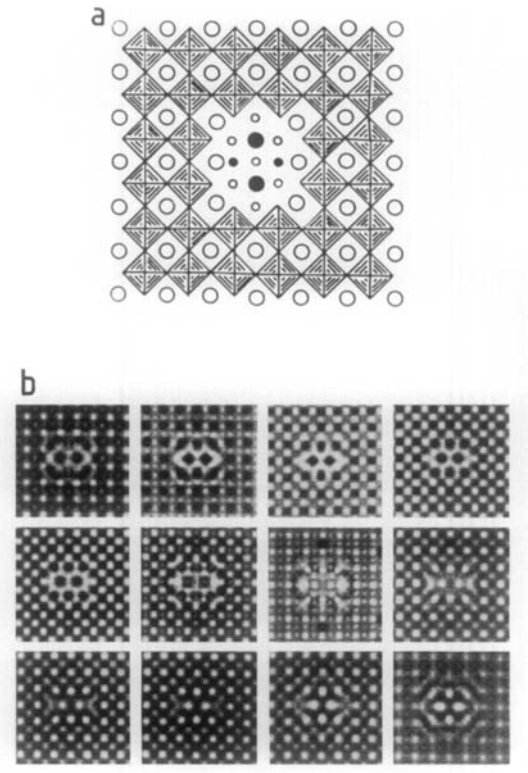

FIG. 10. (a) Model for small defect clusters visible in Fig. 9. Large filled circles Bi at $z = 0$; large open circles Bi at $z = \frac{1}{2}$; small filled circles ● at $z = 0$; small open circles ○ at $z = \frac{1}{2}$. (b) Image simulations for the defect cluster at a thickness of 40 Å and a defocus range of −100 to −1200 Å (575 kV; C_s = 2.50 mm).

displaced in opposite senses from the ideal sites. This is represented in a nonquantitative, idealized manner in Fig. 11b, the effect being best seen by viewing the diagram (and also the micrograph in Fig. 11a) *along* the *a*-direction.

Discussion

The possibility of deriving a hitherto unknown crystal structure (*type*) directly from electron micrographs is a challenging one: most of the published reports describing this kind of application have dealt with variants based on *known* structure types, e.g., "block" structures (see, e.g., *9*), hexagonal "perovskite" polytypes (see, e.g., *10*), tungsten bronzes (see, e.g., *11*), and others. In the present case, the new structure is based on a new principle. In deducing the model for the SL layers, certain geometrical and chemical constraints had to be satis-

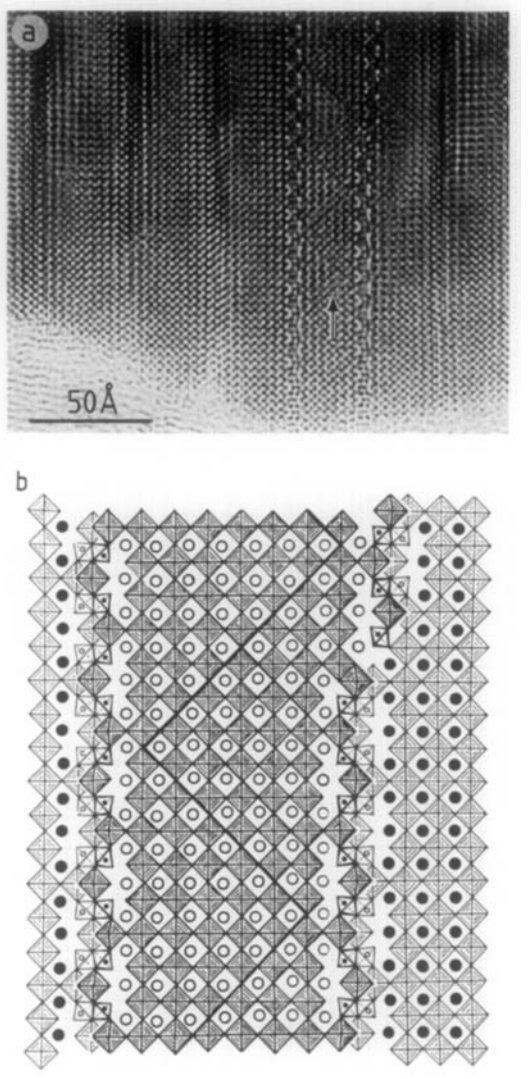

FIG. 11. (a) Chevron contrast along perovskite slabs in an intergrowth of SL and Aurivillius structures. Recorded at 300 kV from the $Bi_{18}Ti_9Fe_{14}O_{66}$ sample. (b) Schematic diagram showing distortions giving rise to chevron contrast.

fied. Because of the inbuilt calibration of the perovskite slabs, accurate dimensions of the repeat unit in the layers could be obtained. The images were obtained under electron-optical conditions which produced dark contrast at projected cation sites. When these cations were located in a structure model, the anion positions were then postulated on a trial and error basis. The most reasonable model was obtained when the oxygen close-packed bismuth sublattice was continued into the SL layer from the perovskite slabs.

The very close relationships between the Aurivillius and the SL structures can be understood if the Aurivillius structure type is described as perovskite slabs separated by a monolayer of close-packed oxygen ions, and if the SL structure is viewed as perovskite slabs interleaved by the three cubic-close-packed oxygen layers comprising transition-metal ions (M) in both octahedrally and tetrahedrally coordinated interstices. Thus, the composition of such a layer incorporating the Bi^{3+} ions becomes $Bi_6M_8O_{18}$, which is comparable to the composition $3 \times Bi_2O_2$ ($a_{SL} = 3 \times d_{110} = 11.7$ Å) in the Aurivillius structure. It is reasonable to assume that the transition-metal ions (M) in the SL layers are Fe^{3+} because that would give the SL layer the formula $(Bi_6Fe_8O_{18})^{6+}$ or $(Bi_2Fe_{8/3}O_6)^{2+}$, i.e., the same charge as the $(Bi_2O_2)^{2+}$ layer in the Aurivillius phase.

It is clear that, like the related Aurivillius phases, the novel structure type described here can form the basis for a homologous series given by the formula

$$(Bi_2Fe_{8/3}O_6)^{2+}(Bi_{n-1}M_nO_{3n+1})^{2-}$$

Some examples derived from this expression are listed in Table I.

The atomic coordinates for the SL layer are obtained from an ideal structure where the mean distance of Fe–O in the tetrahedra is 1.87 Å, whereas the mean Fe–O distance in each edge-sharing octahedra is 1.96 Å. Tetrahedrally coordinated Fe^{3+} has earlier been observed in, for example, $Ca_2Fe_2O_5$ (*12*) in which the corresponding mean values are 1.878 and 2.016 Å, and it is also known in magnetite, but the polyhedral framework of octahedra and tetrahedra is different.

TABLE I

n (number of octahedra in perovskite slab width[a])	Composition	b (Å)
3	$Bi_{12}Ti_9Fe_8O_{48}$	40.0
4	$Bi_{15}Ti_9Fe_{11}O_{57}$	47.8
5	$Bi_{18}Ti_9Fe_{14}O_{66}$	55.6

Note. In all cases the ideal values for a_0 and c_0 are taken to be 11.7 and 3.93 Å, respectively.

[a] Note that, for $n \geq 3$ in the Bi–Ti–Fe–O system, the homologous series is either of the "SL" or of the Aurivillius type.

Conclusion

We have succeeded in deducing a new crystal structure type directly from high-resolution electron micrographs. When the positions of projected cation rows are defined in a structure image, crystal chemical reasoning may provide sensible clues about the likely positions of the anions. With electron microscopes now capable of resolutions in the range 1.5–2 Å, the prospects for wider applications of high-resolution electron microscopy to crystal structure analysis are encouraging.

Acknowledgments

This work has been supported by the Swedish Natural Research Council, the Science and Engineering Research Council (UK), and the National Science Foundation Grant DMR-8306501.

References

1. B. AURIVILLIUS, *Ark. Kemi* **1,** 463 (1949).

2. J. L. HUTCHISON, J. S. ANDERSON, AND C. N. R. RAO, *Proc. R. Soc. London A* **355,** 301 (1977).
3. I. H. ISMAILZADE, *Sov. Phys. Crystallogr.* **12,** 400 (1967).
4. S. HORIUCHI, K. MURAMATSU, AND M. SHIMAZU, *J. Solid State Chem.* **34,** 51 (1980).
5. D. J. SMITH AND J. L. HUTCHISON, *J. Microsc.* **129,** 285 (1983).
6. D. J. SMITH, R. A. CAMPS, L. A. FREEMAN, M. A. O'KEEFE, W. O. SAXTON, AND G. J. WOOD, *Ultramicroscopy* **18,** 63 (1985).
7. M. A. O'KEEFE, P. R. BUSECK, AND S. IIJIMA, *Nature (London)* **274,** 322 (1978).
8. T. J. WHITE, R. L. SEGALL, J. C. BARRY, AND J. L. HUTCHISON, *Acta Crystallogr. Sect. B* **41,** 93 (1984).
9. S. IIJIMA AND J. G. ALLPRESS, *Acta Crystallogr. Sect. A* **30,** 22 (1974).
10. J. L. HUTCHISON AND A. J. JACOBSON, *J. Solid State Chem.* **20,** 417 (1977).
11. S. IIJIMA, *in* "Proceedings, 30th Annu. Meet. of Electron Microscopy Society of America" (C. J. Arceneaux, Ed.), Claitor's, Baton Rouge (1972).
12. A. A. COLVILLE, *Acta. Crystallogr. Sect. B* **26,** 1469 (1970).